Characterizing two types of zonation within slag rims of aged alkali-activated slag pastes through SEM and TEM

Zhang, Yu; Zhang, Shizhe; Liu, Chen; Çopuroğlu, Oğuzhan

DOI
10.1016/j.cemconres.2023.107409

Publication date
2023

Document Version
Final published version

Published in
Cement and Concrete Research

Cement and Concrete Research 176 (2024) 107409

Contents lists available at ScienceDirect

Cement and Concrete Research

journal homepage: www.elsevier.com/locate/cemconres

Characterizing two types of zonation within slag rims of aged alkali-activated slag pastes through SEM and TEM

Yu Zhang [a,b], Shizhe Zhang [b,c], Chen Liu [b], Oğuzhan Çopuroğlu [b,*]

[a] Key Laboratory of Concrete and Prestressed Concrete Structures of the Ministry of Education, Southeast University, Nanjing 210096, China
[b] Microlab, Section of Materials and Environment, Faculty of Civil Engineering and Geosciences, Delft University of Technology, Delft, the Netherlands
[c] Renewi Mineralz & Water, Vlasweg 12, 4782 PW Moerdijk, the Netherlands

ARTICLE INFO

Keywords:
Alkali-activated slag
Slag rim
Zonation
Carbonation
Capillary pore
SEM and TEM

ABSTRACT

In this paper, the authors characterized two types of zonation within slag rims in aged alkali-activated slag (AAS) systems through SEM and TEM technology. These two elemental zonation were closely related to the pore structure of AAS pastes, thus providing strong implication for the transport- and durability-related performance of AAS systems. The first type of zonation occurred in the rims of AAS specimens under sealed curing. It was found that lath-like hydrotalcite-like phase accumulated near the boundary while a generally homogeneous and foil-like C-(N-)A-S-H gel phases precipitated in the following sub-zone. When slag rims were thick enough, a new Mg-rich region occurred. The second type of zonation was noticed in the carbonated AAS pastes. For this kind of distribution pattern, C-(N-)A-S-H gel phases were observed near the boundary. Following, the accumulation of Mg and Ca occurred alternatively. Additionally, transformation mechanism between these two types of zonation was also proposed.

1. Introduction

Blast furnace slag (*slag* for short) is the waste of steelmaking industry. At a temperature of around 1450 °C, the raw iron ore gangues, reduced substances, and components of melted coke are combined to form liquid slag in the blast furnace, and it is referred to as a $CaO\text{-}SiO_2\text{-}Al_2O_3\text{-}MgO$ system [1]. The fine ground slag has been widely used in Europe, North America, etc. for partial replacement of cement clinker [2–4]. Additionally, it has also been used as raw material in alkali-activated systems, such as alkali-activated slag (AAS). Together with a suitable activator, AAS can develop desirable properties [5–8].

Slag hydration in alkaline solution is generally accepted to follow a dissolution-precipitation-diffusion mechanism [9]. The dissolution-precipitation mechanism governs the process at an early age [10,11]. Ion diffusion mechanism controls the continuous hydration of unreacted slag particle at a later age when it has been covered by precipitations [12]. Depending on the alkaline source, hydrotalcite-like phase, C-A-S-H gel phases in cement-based systems [13] or C-(N-)A-S-H gel phases for alkali-activated mixtures [14–18] have been confirmed as the hydration products of slag itself.

Meanwhile, these hydrates only precipitate within the initial perimeter of slag, where they are mixed and called as 'inner' hydration products of slag, also termed as '*slag rim*' [13]. According to Transmission Electron Microscope (TEM) observations, a fine-textured inner products was noted [19–23]. Among them, the plate- or lath-like morphology, indicated the precipitation of hydrotalcite-like phase, was commonly found [22,23]. On the other hand, contradictory opinions regarding the distribution pattern of hydrates in the slag rim do exist in the literature. Based on TEM and Scanning Electron Microscope (SEM) observations, Ye [24] considered that hydrotalcite-like phase (electropositive) and C-A-S-H gel phase (electronegative) were strongly attracted to each other in the rim of slag. The results in [25] also pointed out that the rims surrounding unreacted slag grains were actually a composite phase of C-A-S-H gel phase and hydrotalcite-like phase. Opposite to intermixture, Li et al. demonstrated that three sub-zones, namely Mg-Al hydrotalcite-like phase, C-A-S-H gel phase, and Ca-Al layered double hydroxide phase, were produced around unhydrated slag particles [26]. According to our earlier investigations [27], the distribution patterns of inner hydrates were strongly related to the initial diameters/sizes of slag particles.

On the other hand, durability-related issues of AAS are still under debate, limiting their applications in engineering practice. Especially for carbonation, researchers have observed a low carbonation resistance of AAS systems compared to conventional Portland cements [6,8,28]. It

* Corresponding author.
E-mail address: O.Copuroglu@tudelft.nl (O. Çopuroğlu).

https://doi.org/10.1016/j.cemconres.2023.107409
Received 16 August 2023; Received in revised form 14 November 2023; Accepted 17 December 2023
Available online 28 December 2023

Table 1
Chemical composition of slag.

Oxide (wt%)	CaO	SiO_2	Al_2O_3	MgO	Fe_2O_3	SO_3	Na_2O	K_2O	LOI[a]
Slag	39.8	35.5	13.5	8.0	0.64	1.0	–	0.33	1.15

[a] Loss on ignition at 950 °C.

Table 2
Mixture design of alkali-activated slag pastes (in gram).

	Slag	SiO_2	Na_2O	Modulus	Water[a]	Liquid/binder (l/b)
Group I	100	6.7	4.8	1.45	38.5	0.5
Group II	50	6.7	4.8	1.45	38.5	1

[a] The pH of the water glass solution used was 14.4, measured by pH meter.

can be assigned to the absence of portlandite, the low Ca/Si ratio of the gel phases, as well as the high alkali content of pore solution in alkali-activated binder. C-(N-)A-S-H gel phases in the matrix decalcified during carbonation to form various carbonates [28]. As for the influence of carbonation on slag rims of AAS, few results are found in the existing literature.

For the regularly distribution pattern of hydrates in the slag rim (also referred to as '*zonation*'), it is always linked to the Liesegang phenomenon occurring in nature. It is a quasi-periodic self-organized precipitation appearing with the movement of reaction front [29]. Through diffusion-controlled migration of reactants, various patterns, including rings (in particular), bands, as well as spheres, are commonly noticed in saturated porous mediums [30]. Two nucleation theories have been summarized to explain various Liesegang patterns: (1) Ostwald's supersaturation theory (i.e., pre-nucleation theory) associated with the cycle of supersaturation-nucleation-depletion [30–32] and (2) competitive particle growth model (i.e., post-nucleation theory) [33–37] with the development of Lifshitz-Slyozov instability [38]. Its occurrence in the hydration of cementitious materials, e.g., fly ash and slag, has also been reported [39–42]. However, very few research have studied the exact composition of each ring, different distribution patterns and corresponding formation mechanisms, as well as their implications for the microstructure of matrix. Besides, according to the best of authors' knowledge, no research focused on the effect of carbonation on the distribution patterns of hydrates within slag rims.

To fill these gaps, the authors in the present study identified two types of zonation in the rims of (partially or completely) hydrated slag grains of aged AAS pastes under different conditions (sealed, naturally exposed, and accelerated carbonation), by means of SEM and TEM. The exact composition of each ring was studied, different distribution patterns of hydrates in the rims were summarized, similarities and differences as well as the possible transformation mechanism between them was explored and discussed. Furthermore, it was found that the formation of different types of zonation in the slag rims was closely related to the pore structure. This provided important insight into transport- and durability-related performance of AAS-based systems, as the transport of various harmful species, including CO_2, chloride, sulfate, etc. was dominated by the pore structure.

2. Materials and methodology

2.1. Materials

The slag adopted in this paper was produced by Ecocem Benelux B. V., the Netherlands. Its chemical composition based on the measurement of X-ray Fluorescence (XRF) is shown in Table 1. In addition, it presented a specific gravity of around 2900 kg/m^3 and its d_{50} was ~19 μm.

Analytical regent sodium hydroxide (purity ≥98 %), liquid sodium silicate solution (8.25 wt% of Na_2O, 27.50 wt% of SiO_2, and 64.25 wt% of H_2O), and distilled water were employed for the preparation of alkaline activator. It was prepared 24 h before casting and allowed to cool down at a room temperature of 20 ± 3 °C.

2.2. Sample information

Two groups of AAS paste were prepared for different curing conditions in the study. Table 2 gives the detailed information of each group. After demoulding, half of the specimens of Group I was naturally exposed to the laboratory environment at a temperature of 20 ± 3 °C and relative humidity (RH) of 50 ± 5 %. The other half was sealed for curing. After about 6 years of curing, all the AAS pastes of Group I were examined in the present research. To reproduce the phenomenon found in long-term natural curing condition with an accelerated test, the authors prepared a new mixture, i.e., Group II as introduced in Table 2. The liquid/binder ratio was enhanced to 1.0 to accelerate the reaction of slag and formation of thick rims around unreacted grains. After 6 months of sealed curing in the same laboratory, they were unsealed and moved to a carbonation chamber. Accelerated carbonation curing was carried out with a CO_2 concentration of 0.5 vol% ± 0.1, at 20 ± 3 °C and 65 ± 5 % of RH. The accelerated carbonation curing lasted for 6 months. Note that increased porosity due to high liquid/binder ratio further promoted the carbonation degree of specimens.

2.3. Experimental methods

The reaction products formed in AAS pastes were characterized by thermogravimetric analysis (TGA) and X-ray diffraction (XRD). Before measurement, representative pastes were crushed into small pieces and the reaction was terminated by solvent exchange with isopropanol. Afterwards, these pieces were ground into fine powder using a mortar and further meshed to below 63 μm. Netzsch STA 449 F3 Jupiter Netzsch QMS 430C was employed for TG analysis. Approximately 50 mg sample powder was heated from 40 to 900 °C (10 °C per min) under an argon atmosphere. XRD data was collected using a Philips PW 1830/40 Powder diffractometer with Cu K-alpha radiation. The machine was operated with an X-ray beam current of 40 mA and an acceleration voltage of 40 kV. Sample powders were scanned from 5 to 60° (2θ) with a step size of 0.03°.

For Mercury Intrusion Porosimeter (MIP) analysis, it was performed with a Micromeritics Autopore IV which determined the pore size down to 7 nm (corresponding to a 0–210 MPa range of applied pressure). After hydration stop, crushed particles were stored in a desiccator under vacuum until constant weight. It should be noted that the surface tension of 0.485 N/m and the contact angle of 140° were used for determining pore size in the paper.

Meanwhile, the polished sections of AAS pastes under different curing conditions were also prepared. After proper grinding and polishing, the surfaces of selected AAS specimens were carbon coated. For back-scattered electron (BSE) images, these carbon-coated samples were examined with a FEI Quanta FEG 650 ESEM under a 10 kV accelerating voltage and a working distance of 10 mm. X-ray energy dispersive detector was also equipped to determine the elemental compositions of phases interested with internal standard (standardless microanalysis).

Additionally, some of the polished surfaces were characterized using TEM. These samples were loaded into a dual-beam FIB-SEM system (Zeiss Crossbeam 540) to precisely navigate slag rims of interest. The schematic illustration of sample preparation with this system is introduced in Fig. 1. After loaded into the equipment (Fig. 1(a)), the region of interest (as indicated by blue rectangle in Fig. 1(b)) was located by

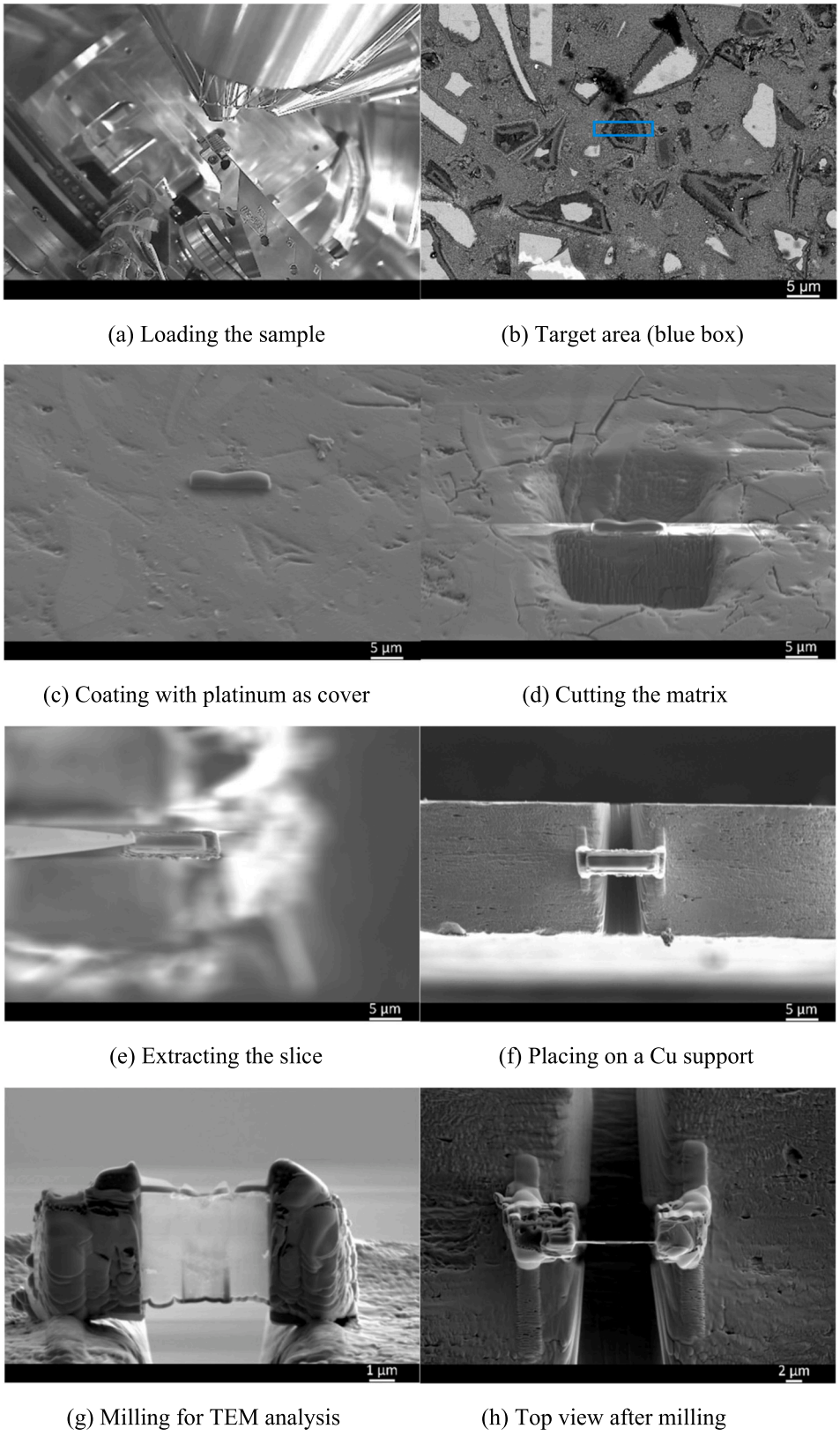

Fig. 1. Schematic illustration of sample preparation for TEM analysis using a dual-beam FIB-SEM system.

means of back-scattered electron (BSE) image. This area was probably originated from a totally hydrated slag grain. Afterwards, it was coated with platinum on the surface, as exhibited in Fig. 1(c). The matrix on the both sides of platinum cover was slowly cut by focused-ion-beam (FIB), using Ga^+ ion (Fig. 1(d)). Subsequently, the target area beneath the platinum cover was extracted from the matrix (the slice in Fig. 1(e)) and transferred to a Cu support as shown in Fig. 1(f). Focused Ga^+ ions were further employed to thin the extracted slice (Fig. 1(g)) and sample with a

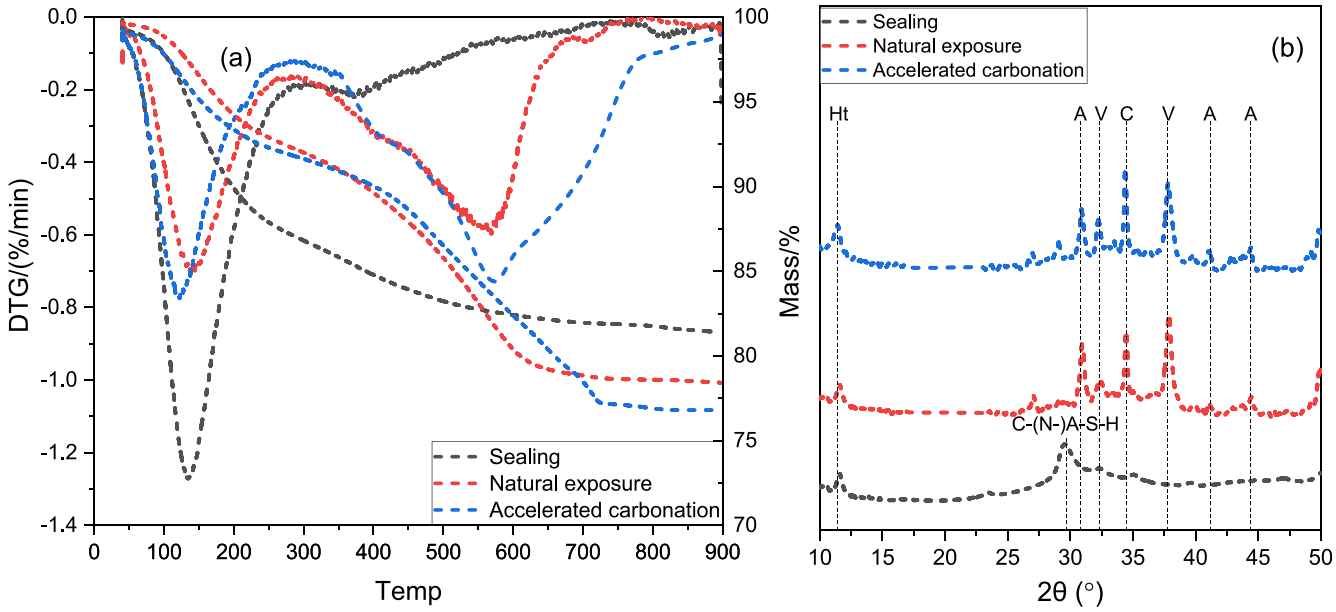

Fig. 2. (a) TG and DTG; (b) XRD results of AAS pastes under different curing conditions. Ht: hydrotalcite-like phase; A: aragonite; C: calcite; V: vaterite.

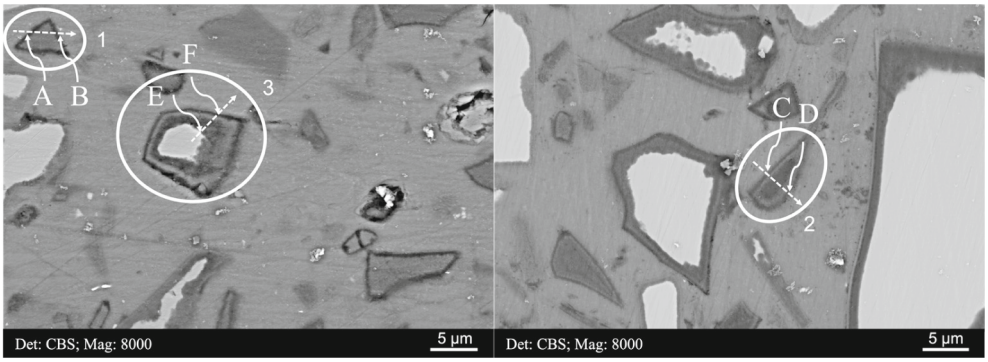

(a) (b)

Fig. 3. (a) and (b) Representative BSE micrographs of the microstructure of alkali-activated slag paste after approximately 6 years of sealed curing.

thickness of ~100 nm was yielded (Fig. 1(h)). One should keep in mind that due to the brittleness of AAS paste, both the accelerated voltage and beam density of focused Ga^+ ions should be kept as low as possible, to minimize the damage caused by milling process [26]. Finally, the nanoscale morphology and elemental compositions of the prepared samples were observed through FEI talos F200X G2 in tandem with a high-angle annular dark-field detector (HAADF).

3. Results and discussion

3.1. Reaction products in AAS pastes under different curing conditions

Fig. 2(a) exhibits the TG and DTG curves along with the identified temperature ranges of AAS samples under different curing conditions. A distinct peak at around 150 °C was found in AAS paste with sealed curing, which can be assigned to the dehydration of gel phases, e.g., C-(N-)A-S-H gel phases [12–14]. A small hump was also identified at ~350 °C, associated with the decomposition of hydrotalcite-like phase. As for the specimens cured naturally in the laboratory, the broad peak starting from about 300 °C corresponded to the release of CO_2 from various metastable to stable carbonates [43,44]. The intensity of decomposition peak for gel phases also decreased remarkably, confirming their carbonation during naturally exposed curing. For specimens with accelerated carbonation curing (Group II), they presented a similar thermal decomposition characteristics to naturally exposed ones. Relatively more carbonates were formed in this blend due to the more severe CO_2 attack, and the greater mass loss was seen between 350 and 900 °C.

XRD results reveal the presence of hydrotalcite-like phase and C-(N-)A-S-H gel phases in AAS paste after sealed curing for around 6 years (Fig. 2(b)). After natural exposure (Group I) or accelerated carbonation curing (Group II), the peak for C-(N-)A-S-H gel phases disappeared, meaning that these specimens had been carbonated. Aragonite, calcite, and vaterite were identified as the main polymorphs of $CaCO_3$ in the carbonated samples. On the other hand, note that hydrotalcite-like phase was still observed after such a heavy CO_2 attack in both groups.

3.2. Zonation under sealed curing (type I)

Fig. 3(a) and (b) displays the representative microstructure of alkali-activated slag paste after approximately 6 years of sealed curing. The microstructure was composed of a mixture of unreacted slag grains, slag rims, and gel matrix. Both fully and partially reacted slag particles can be observed throughout the matrix and distinguished by their thick rims and/or unreacted cores. Overall, these observations suggested that the long-term sealed curing process had resulted in a well-developed

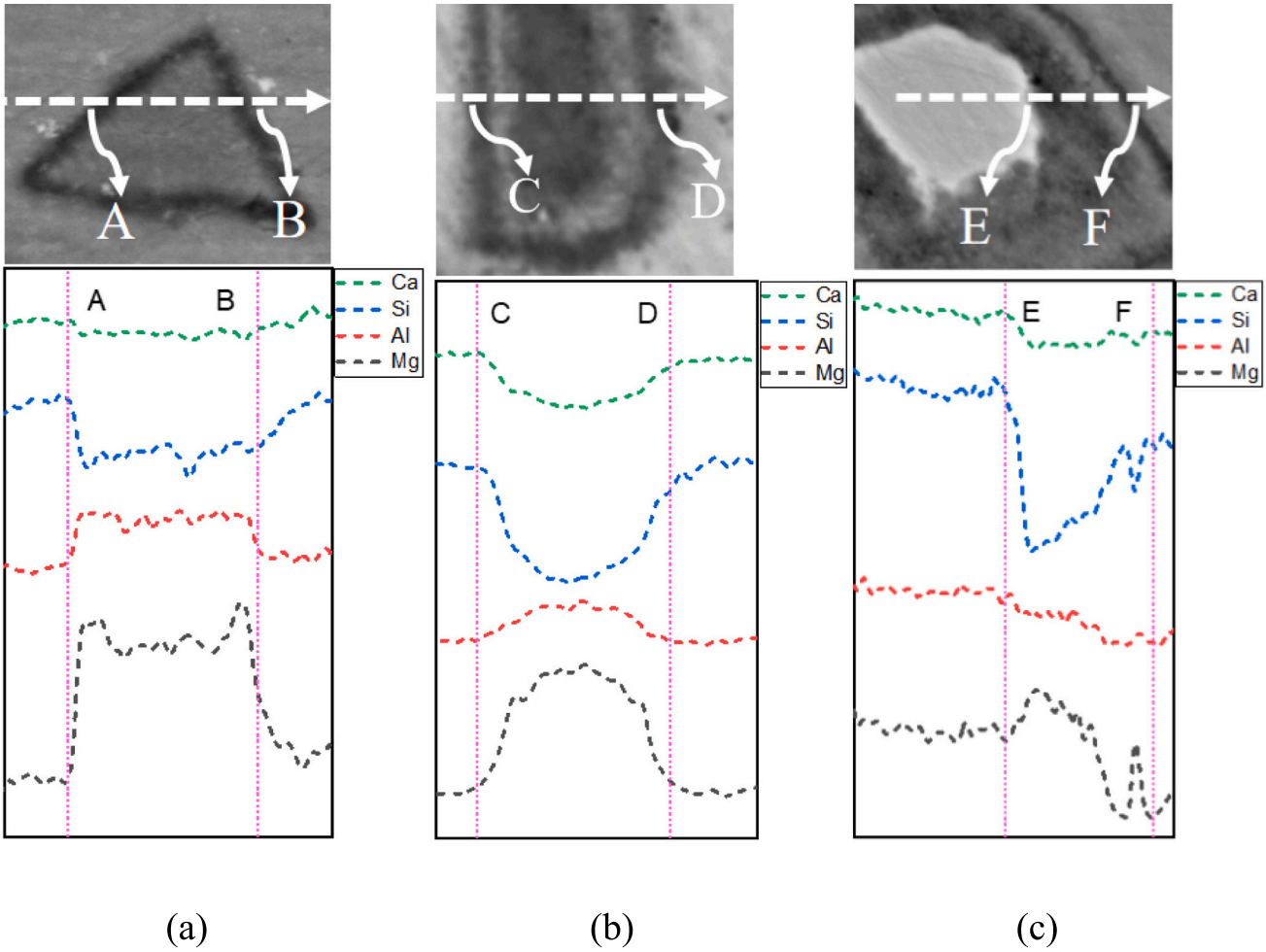

Fig. 4. Linescan-profiles of Ca, Si, Al and Mg (atomic %) along the dissection lines (a) A–B, (b) C–D, and (c) E–F shown in Fig. 3.

microstructure with a high reaction degree of slag.

Fig. 4(a)–(c) reveals the linescan-profiles (atomic ratio) of main elements along the dissection lines A–B, C–D, and E–F in Fig. 3, respectively. Two distinct areas were observed upon the full hydration of slag grain in circle 1. A clear increase in Mg and Al concentrations while a decrease in Si content was noticed near the boundary. Conversely, the concentration of Mg went down when approaching the core (Fig. 4(a)). Unlike the slag grain in circle 1, an even higher magnesium concentration was measured in the center of slag grain in circle 2, as Fig. 4(b) shows. Additionally, most Ca and Si ions had migrated out, indicated by the significant drop of their concentrations when moving to the middle. As for the partially hydrated slag grain in circle 3, three areas were clearly visible. The boundary abundant in Mg appeared dark; the adjacent sandwiched zone presented a less dark coloration, as Ca and Si concentrations rose in this area. When approaching inside further, a new region also enriched in Mg and scarce of Si occurred, surrounding the unreacted slag particle (Fig. 4(c)).

This type of zonation under sealed curing was similar to that observed in aged cement-slag system in [27]. It mainly presents two distinctive features: (1) Magnesium is always accumulated near the boundary of slag particle, irrespective of its original size/shape; and (2) when the rim is thick enough, a new region also rich in Mg is formed in the core or surrounding the unreacted slag grain. However, note that a certain amount of magnesium was still trapped in the core of fully hydrated small slag grain (Fig. 4(a)). Compared to specimen investigated in [27], where no magnesium was detected in the center of fully hydrated small slag grain, the curing age of AAS paste examined in this paper was relatively shorter. It would take longer time for the stable hydrotalcite-like phase precipitated near the boundary to consume nanometer-sized hydrotalcite-like phase (amorphous or microcrystalline) formed in the core. This process was also known as Ostwald ripening [45].

Moreover, TEM analysis was used in this study to exhibit and understand the morphology and composition of this type of zonation at nano-scale. The target area, indicated by the rectangle in Fig. 1(b), was employed as a representative example. As can be seen, this region was most probably a result of a completely reacted slag grain, and it presented a similar appearance to that circled in Fig. 3(b), i.e., the boundary and core were abundant in magnesium with relatively dark coloration while the sandwiched zone exhibited the almost same coloration of gel matrix.

Fig. 5(a) illustrates the overall morphology of the interested zone beneath the platinum cover. Three sub-zones with hydrates presenting intrinsic differences in morphology at nano-scale level can be identified. The interface between the outer and inner products, i.e., the initial boundary of the slag grain, can be distinguished clearly and is marked by the solid line in the graph. Magnified images of the small area P1 are shown in Fig. 5(b1) and (b-2), to represent the sub-zone near the boundary. Numbers of fringes, indicated by the red boxes in Fig. 5(b-1), implied the presence of ordered atomic planes stacking of phases that precipitated here. Additionally, they mainly exhibited a distinct lath-like morphology as seen in Fig. 5(b-2), corresponding to the formation of hydrotalcite-like crystal [22,23]. Two evident electron diffraction spots (R1 and R2) were detected in the fast Fourier transform (FFT) pattern (Fig. 5(b-3)). The corresponding mean basal spacing (measured from inverse fast Fourier transform (IFFT) pattern) was ~0.7520 and

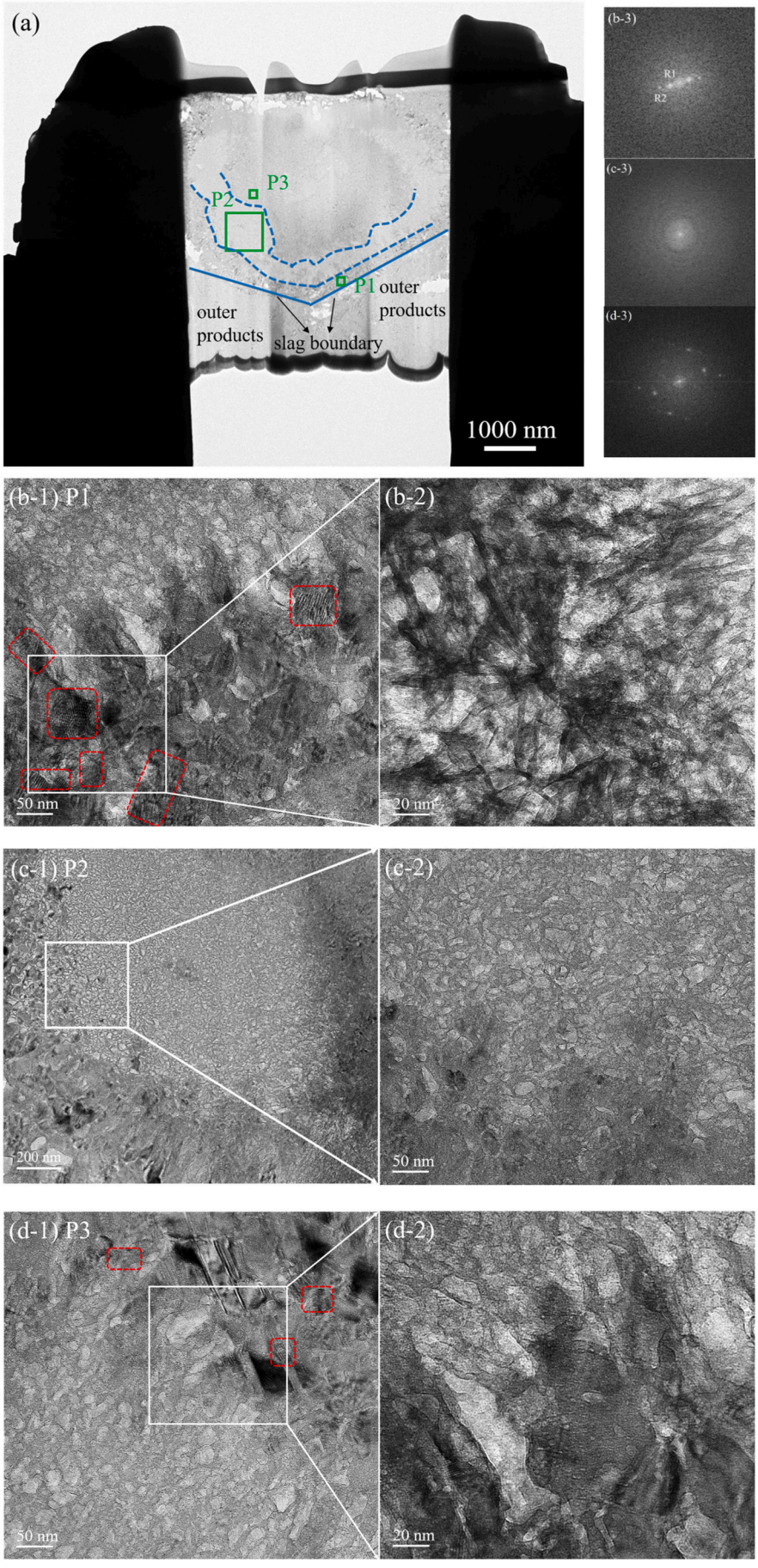

(caption on next page)

Fig. 5. TEM analysis of hydrates in the rim of slag; (a) the overall morphology of target area beneath the platinum cover; (b-1) enlarged image of the area P1 in (a); (b-2) magnified image of the area marked by the white box in (b-1); (b-3) the FTT pattern of hydrotalcite-like phase; (c-1) zoomed in image of the area P2 in (a); (c-2) magnified image of the area marked by the white box in (c-1); (c-3) the FTT pattern of C-(N-)A-S-H gel phases; (d-1) enlarged image of the area P3 in (a); (d-2) magnified image of the area marked by the white box in (d-1); (d-3) the FTT pattern of nanocrystalline hydrotalcite-like phase.

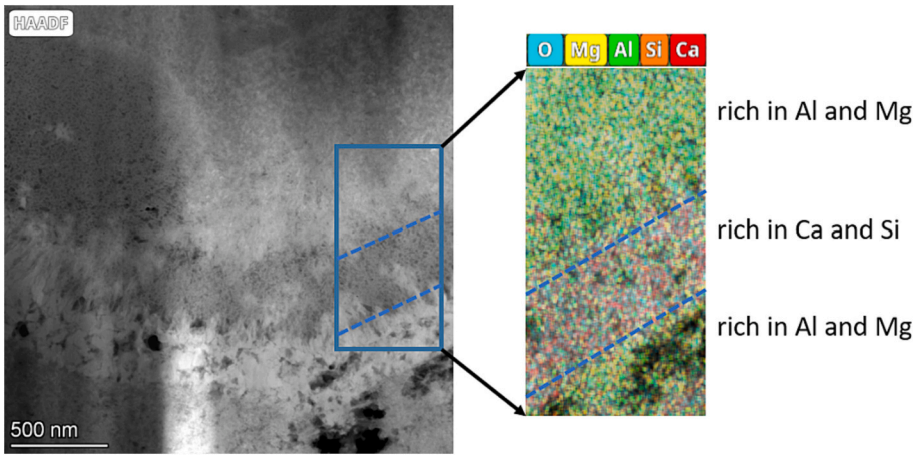

Fig. 6. The HAADF micrograph and main element mappings of Ca, Si, Al, and Mg covering three sub-zones in the rim.

~0.3742 nm, respectively. These values agreed well with the basal spacing $d_{(003)}$ and $d_{(006)}$ of various hydrotalcite phases [25].

On the other hand, a generally fine and homogeneous morphology was observed in the area P2 in Fig. 5(c-1). The foil-like morphology of the hydration products identified in this sub-zone shown in Fig. 5(c-2) corresponded to that of C-(N-)A-S-H gel phases as reported in [23]. No lattice fringe and the absence of obvious diffraction spot in the FFT pattern (Fig. 5(c-3)) confirmed that C-(N-)A-S-H gel phases formed in the sandwiched zone was largely disordered. Moving forward to the core in the area P3 displayed in Fig. 5(d-1), fringes (not well ordering) indicated by the red boxes were observed again. However, compared to those identified in area P1, (most probable) hydrotalcite-like phase precipitated in this sub-zone was nanocrystalline or at least with much lower crystallinity. It was supported by the irregular diffraction spots occurred in the FFT pattern in Fig. 5(d-3).

Fig. 6 presents the HAADF micrograph and main element mappings of Ca, Si, Al, and Mg covering three sub-zones in the rim. The enrichment of Al and Mg near the boundary and in the middle part verified the presence of hydrotalcite-like phase (crystalline and/or nanocrystalline), which was in line with previous TEM analysis. The sandwiched zone was abundant in Ca and Si, which were two main components of highly disordered C-(N-)A-S-H gel phases formed in this sub-zone.

To summarize, both morphology observation and element distribution supported the zonation of hydration products within slag rim at nano-scale. This type of zonation was featured by the accumulation of magnesium, or the formation of hydrotalcite-like phase near the boundary. When the thickness of slag rim increased, exceeding the migration ability of Mg^{2+} ion, magnesium accumulated locally and formed a new region also rich in Mg in the core or surrounding the unreacted core, in the form of nanocrystalline hydrotalcite-like phase. Besides, this schematic summary of zonation in sodium silicate based AAS system that had been sufficiently cured in a sealed condition was consistent with that based on cement-slag system (Fig. 15 in [27]). Admittedly, the pH of pore solution is significantly higher in AAS mixture compared to slag cement paste, and it can exert a considerable influence on the hydration rate and reaction degree of slag [46–49]; however, it does not change the ultimate distribution of hydrates in the rim of slag grain.

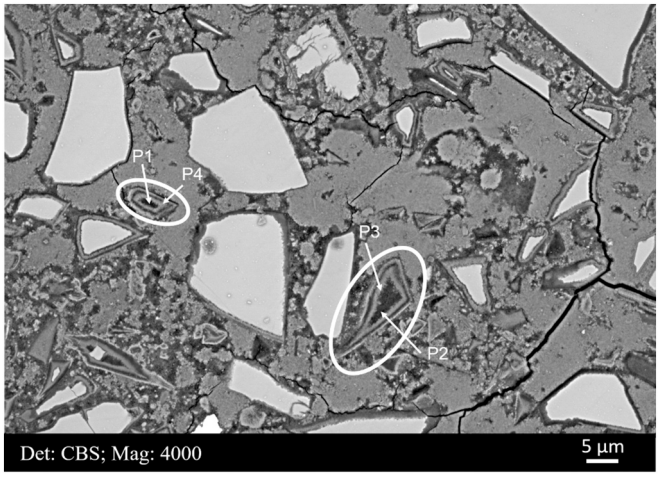

Fig. 7. Representative BSE micrograph of the microstructure of sodium silicate based AAS paste after ~6 years of natural curing.

3.3. Zonation under naturally exposed and accelerated carbonation curing (type II)

3.3.1. Multi-ring phenomenon occurred in AAS paste after naturally exposed curing

Fig. 7 displays the representative microstructure of sodium silicate based AAS paste after being naturally exposed in the laboratory for about 6 years. According to the DTG results in Fig. 2, these specimens had already been (totally) carbonated after such a long curing age. The matrix appeared very porous, with numbers of black spots indicating the formation of pores due to the carbonation and the resulting shrinkage of gel phases [50–52]. Most slag grains, either partially or fully hydrated, seemed to be separated from the gel matrix, implied by the presence of pores along the slag perimeter. Furthermore, the distribution of hydrates within slag rims was notably chaotic. Under this circumstance, the zonation of hydrates in the slag rim under sealed curing did not apply anymore.

Instead, a multi-ring phenomenon was frequently observed in the rims of fully hydrated slag grains as circled in Fig. 7. A similar

Table 3
EDS point analysis results (atomic percentage, %).

	Ca	Si	Al	Mg	Mg/Al
P1	3.32	7.21	7.19	10.54	1.47
P2	1.22	9.64	9.35	12.38	1.32
P3	11.49	8.01	5.34	7.57	1.42
P4	8.05	9.59	5.21	7.32	1.40

phenomenon was also reported in [42], in which the microstructure of a 7-year-old AAS concrete was tested. Unlike zonation of Type I (Section 3.2), this type of zonation (Type II) exhibited its own distinctive features of both morphology and composition, which would be elaborated in this section.

The chemical compositions of selected points (P1 to P4) determined by EDS are reported in Table 3. Evidently, point P1 and P2 were rich in magnesium while deficient in calcium, in line with the relatively dark

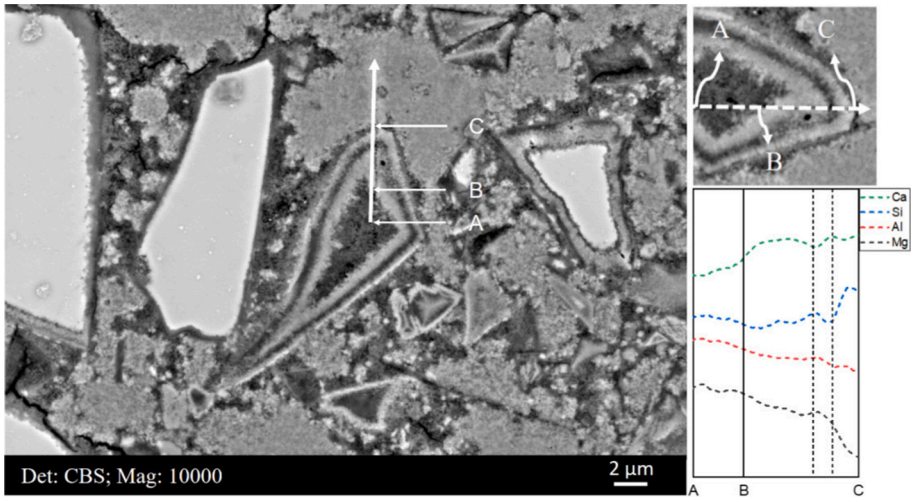

(a) (b)

Fig. 8. (a) Enlarged image of multi-ring phenomenon occurred in a fully hydrated slag grain; (b) Linescan-profiles of Ca, Si, Al and Mg along the dissection lines A–C in (a).

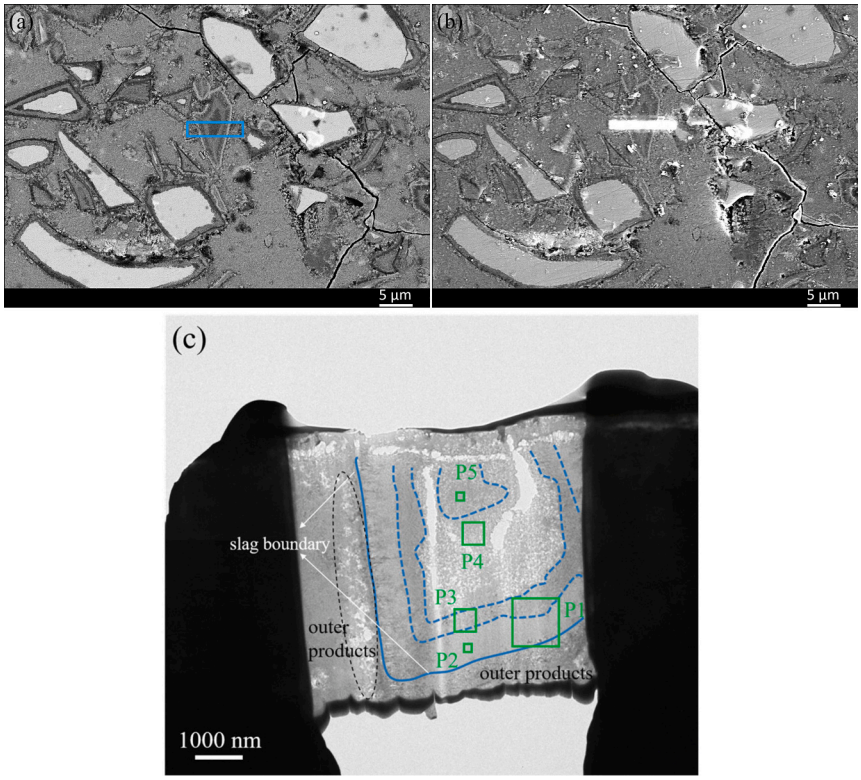

Fig. 9. TEM analysis of hydration products in the concentric ring structure; (a) BSE image of the interested area; (b) coating the area with platinum cover; (c) the overall morphology of hydrates beneath the platinum cover; (d) magnified image of the area P1 in (c); (e) zoomed in image of the area P2 in (c); (f) enlarged image of the area P3 in (c); (f-1) magnified image of the area marked in (f); (g) magnified image of the area P4 in (c); (h) zoomed in image of the area P5 in (c).

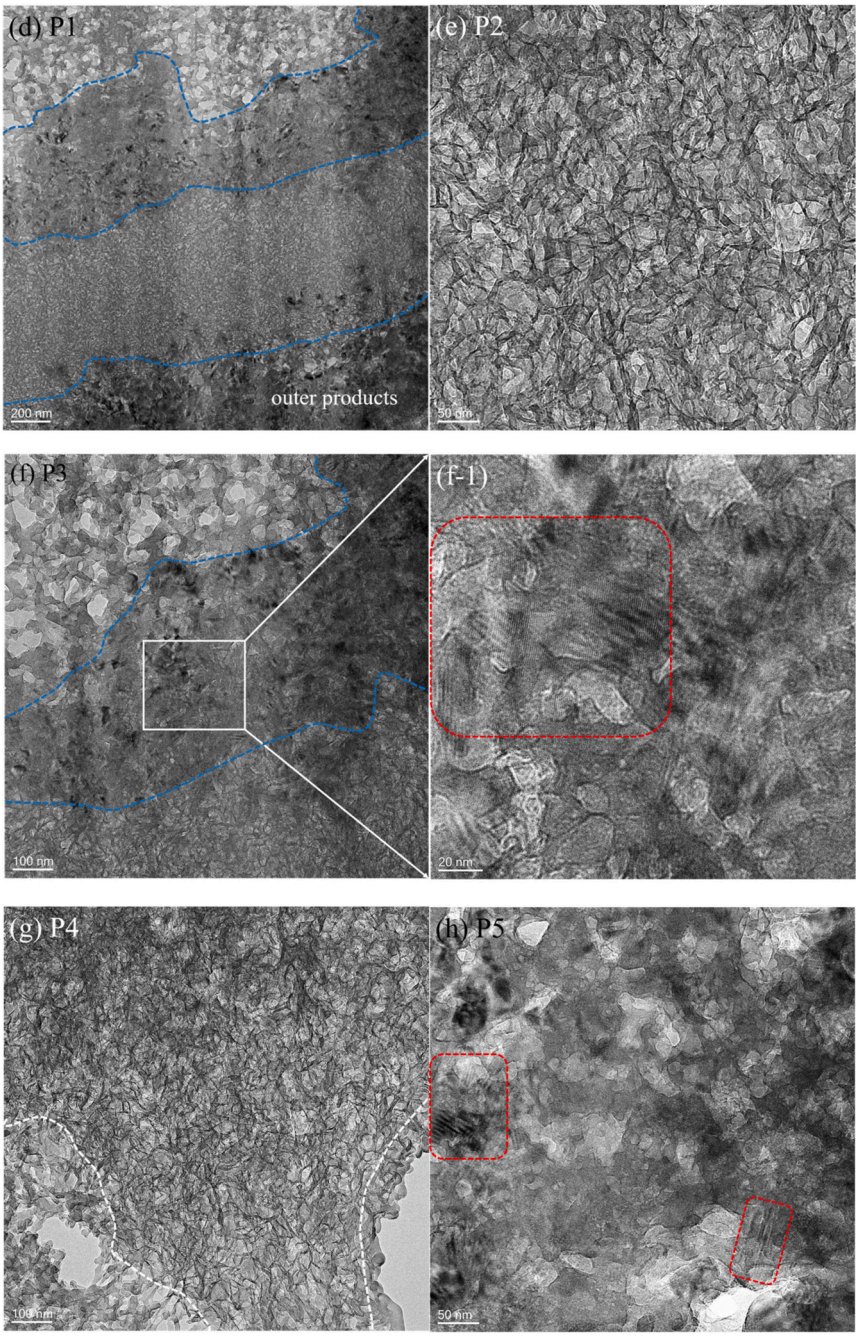

Fig. 9. (*continued*).

coloration in the core areas in the BSE image. On the contrary, the relatively grey (lighter coloration) areas sandwiched between the core and dark band, where point P3 and P4 were located, were abundant in calcium. The Mg/Al atomic ratio appeared to level off for all four points, fluctuating at ~1.40.

Fig. 8(b) reveals EDS linescan-profiles (atomic ratio) of main elements along the concentric ring structure occurred in Fig. 8(a). Basically, the Mg concentration presented a clear decline trend, while a slight rising trend was seen for Ca from inside to outside (A to C). The central zone of this completely hydrated slag grain illustrated a high Mg concentration while a relatively low concentration of Ca, in agreement with the point analysis results of P1 and P2. Moving along the dissection line to the dark band between B and C (isolated by two dash lines in Fig. 8(b)), a slight reduction of Ca and Si contents whereas a small increase of Mg amount was noticed. As for the sandwiched area between the core and dark band, the Ca content rose, agreed well with the point analysis results of P3 and P4.

Next, the morphology and composition of this concentric ring structure was examined at a nano-scale level through TEM. The area of interest (a new example with a similar distribution pattern to those circled in Fig. 7) was marked by the rectangle in Fig. 9(a). Sub-zones with relatively grey and dark colorations occurred alternatingly from outside towards inside.

Fig. 9(c) illustrates the overall morphology of target area beneath the platinum cover. The boundary (solid line) between inner and outer products of slag particle can be distinguished. Pores, as circled in the graph, were detected along the grain perimeter. In other words, the inner products of slag particle were not compacted closely with outer products, and they were separated from each other. It was consistent with the observations based on BSE images (Fig. 7).

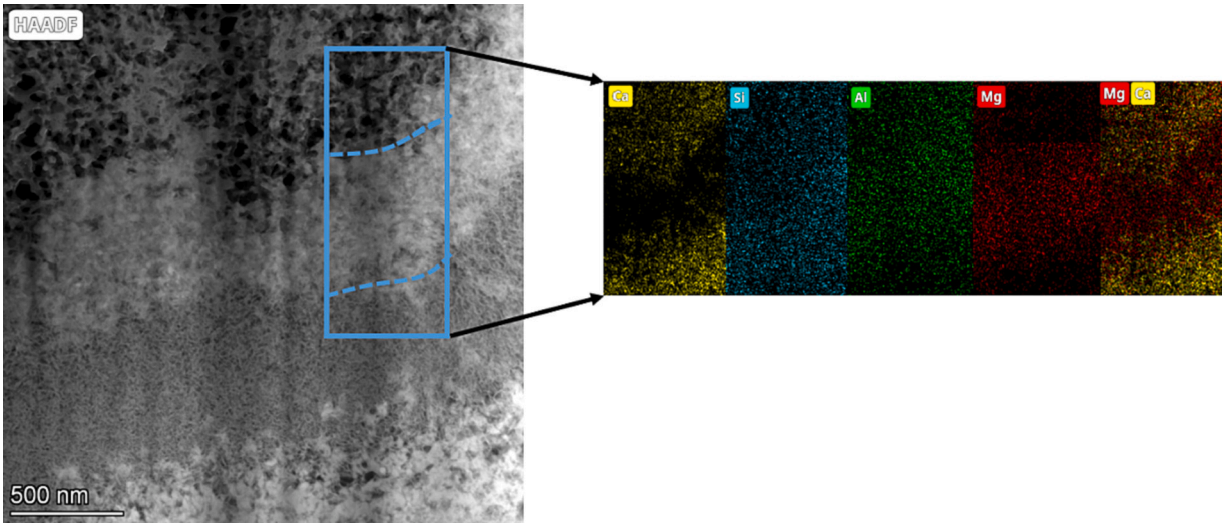

Fig. 10. The HAADF micrograph and main element mappings of Ca, Si, Al, and Mg covering three sub-zones in the slag rim.

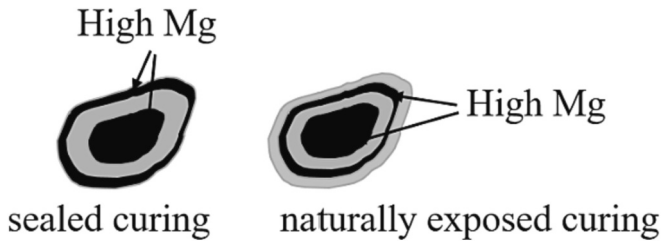

Fig. 11. A schematic comparison between these two types of zonation formed in the rim of slag.

Moreover, C-(N-)A-S-H gel phases, instead of hydrotalcite-like phase (Fig. 5), was found near the initial boundary of slag grain in the area P1 (Fig. 9(d)). Its foil-like morphology was seen clearly in the enlarged image in Fig. 9(e), where P2 was situated. Moving inside further to the next sub-zone (P3), numbers of fringes, marked by red boxes in Fig. 9(f-1), suggested the massive precipitation of hydrotalcite-like phase here.

When approaching the sandwiched area P4 (Fig. 9(g)), it appeared to be much more porous than other sub-zones. Two different morphologies of C-(N-)A-S-H gel phases were seen in this region, i.e., a globular morphology at the corners and a foil-like morphology in the center as isolated by dash lines in the graph. According to previous studies [53], C-(N-)A-S-H gel phases presenting globular morphology were thermodynamically unstable and can be regarded as precursors. They would transform into the well-known foils gradually. On the other hand, silica gel, the carbonation product of C-(N-)A-S-H gel phases, also exhibited a globular morphology as reported in [54].

Moving to the center part, i.e., the area P5, fringes were noticed again and were marked by red squares in Fig. 9(h). Due to the low mobility of Mg^{2+} ion [55], the newly released magnesium ions cannot reach outside and precipitated locally as a new Mg-rich region, which appeared as the dark core in Fig. 9(a).

Fig. 10 displays a close-up HAADF micrograph of a representative region in Fig. 9(c), as well as the main element mappings covering three sub-zones in the slag rim. As can be seen, amounts of black spots, implying the presence of pores, were found in the sandwiched region under HAADF mode. On the other hand, unlike the observations on slag rims under sealed curing (Fig. 6), a significant deficiency of Mg while a high Ca concentration was noticed near the boundary. Meanwhile, the accumulation of Mg and Ca occurred alternatively in the following areas, which agreed with the EDS linescan results exhibited in Fig. 8(b). The distribution of Si and Al, on the other hand, seemed to occupy the whole region. Overall, the morphology observation and elemental distribution results matched well with each other, both of which supported the concentric ring structure of this type of zonation in the slag rim at nano-scale.

A schematic comparison was made in Fig. 11 between these two types of zonation occurred in AAS under different curing conditions, i.e., sealed and naturally exposed curing. Two obvious differences emerged: (1) The boundary of slag grain was rich in magnesium while deficient in calcium under sealed curing; however, it was rich in calcium while deficient in magnesium under naturally exposed curing. No Mg accumulation was detected near the boundary in the multi-ring phenomenon (concentric ring structure). (2) Under sealed curing, slag boundary was connected with the matrix closely, rendering as a transition area between gel phases formed in the matrix and hydration products in the rim of slag. However, slag hydrates in the concentric ring structure seemed to be detached from the matrix, and pores were formed along the perimeter of original slag grain. At the same time, a number of pores were also observed in the slag rim, coexisting with C-(N-)A-S-H gel phases. On the other hand, similarities were also identified between these two types of zonation, e.g., the core was always rich in magnesium; the regions rich in magnesium and calcium were formed alternatingly.

3.3.2. *Multi-ring phenomenon occurred in AAS paste after accelerated carbonation curing*

Fig. 12(a) displays the representative microstructure of AAS paste of such a high liquid/binder ratio after 6 months of sealed curing. As can be seen, it exhibited similar features to AAS paste after ~6 years of sealed curing. Both fully and partially hydrated slag particles were observed throughout the matrix. Due to the high liquid/binder, continuous crack networks were also developed.

Then, an accelerated carbonation curing was performed for these specimens for another 6 months, and the representative microstructure is present in Fig. 12(b). Similar to the observations in Fig. 7, these samples exhibited a highly porous matrix and a chaotic distribution of secondary precipitations within the slag rim after carbonation curing. Again, the concentric ring structure was seen as circled in the BSE micrograph in Fig. 12(c).

3.4. *Transition state due to carbonation*

As mentioned, massive pores were formed along the perimeter of original slag grains due to carbonation (for both naturally exposed and accelerated carbonation curing). Fig. 13 reports the MIP results of all AAS pastes examined in the present research. For specimens that

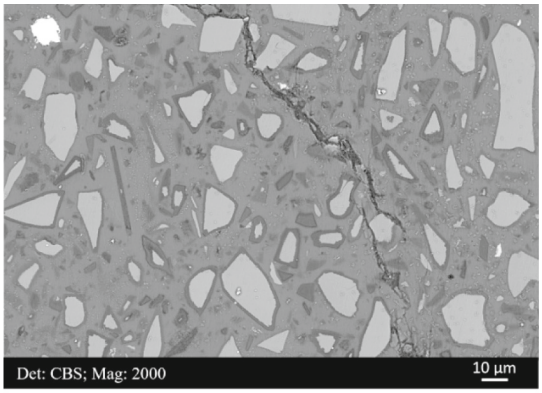

(a)

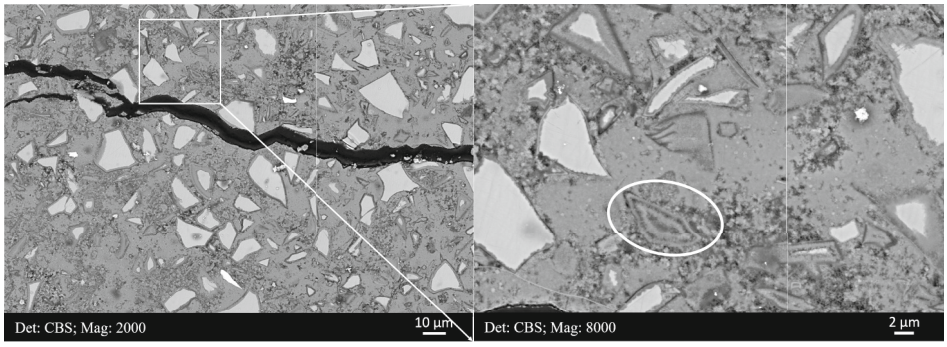

(b) (c)

Fig. 12. Representative BSE micrographs of the microstructure of AAS paste (l/b = 1.0) (a) after 6 months of sealed curing; (b) after another 6 months of accelerated carbonation curing; (c) zoomed in image of the area in (b).

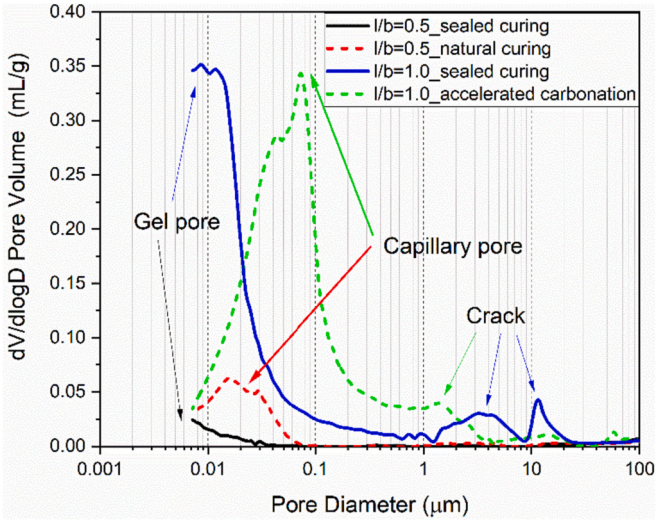

Fig. 13. Differential pore size distribution of all AAS pastes examined in the present research.

underwent sealed curing, regardless of l/b ratio (0.5 or 1.0), the pore structure was dominated by gel pore, with a critical pore diameter at ~10 nm (l/b = 1.0) or even less (l/b = 0.5). The microstructure became coarser owing to the carbonation of C-(N-)A-S-H gel phases, and the critical pore diameter accordingly shifted right to the pore size range of capillary pore (10 to 100 nm). This finding was consistent with the BSE images shown in Figs. 7 and 12(b), where the gel matrix appeared to be very porous after carbonation.

A typical slag rim after CO_2 ingress is illustrated in Fig. 14(a). The pores implied by the black spots inside the rim suggested that the rim was very porous. Besides, pores were formed along slag perimeter, most probably because of the carbonation and thus shrinkage of C-(N-)A-S-H gel phases in the matrix. Following, carbonate ions (CO_3^{2-}) initially in the pore solution of matrix were able to diffuse into slag rim through these pores. They would further react further with C-(N-)A-S-H gel phases precipitated in the rim, thus facilitating the formation of pores and disrupting the original distribution pattern of inner hydrates (Fig. 14(a)). Meanwhile, cations, e.g., Ca^{2+}, Si^{4+}, Al^{3+}, and Mg^{2+} ions can migrate relatively freely because of the increased porosity. The above reasoning was supported by results reported in [56] that gel phase with lower Ca content tended to exhibit a higher porosity than Ca-rich gel.

The EDS linescan-profiles of chosen elements along the dissection line A–B in (a) are given in Fig. 14(b). In general, the Na and O concentrations increased continuously from inside to outside. The O concentration presented a sudden drop near the boundary, which confirmed the formation of pores along the slag perimeter. Except a small increase near the unreacted slag grain, the content of Mg decreased along the dissection line. No accumulation of Mg near the boundary was detected anymore. In short, all elements presented a gradual increase or decrease trend when moving outward from unreacted slag grain, without any accumulation of a specific element at a specific location.

Fig. 15 elaborates the TEM analysis of a representative slag rim in AAS paste which had already been attacked by CO_2. No regular distribution pattern of inner hydration products can be observed (Fig. 15(a)), and they presented similar characteristics to Fig. 14. The overall morphology of this typical slag rim beneath the platinum cover was

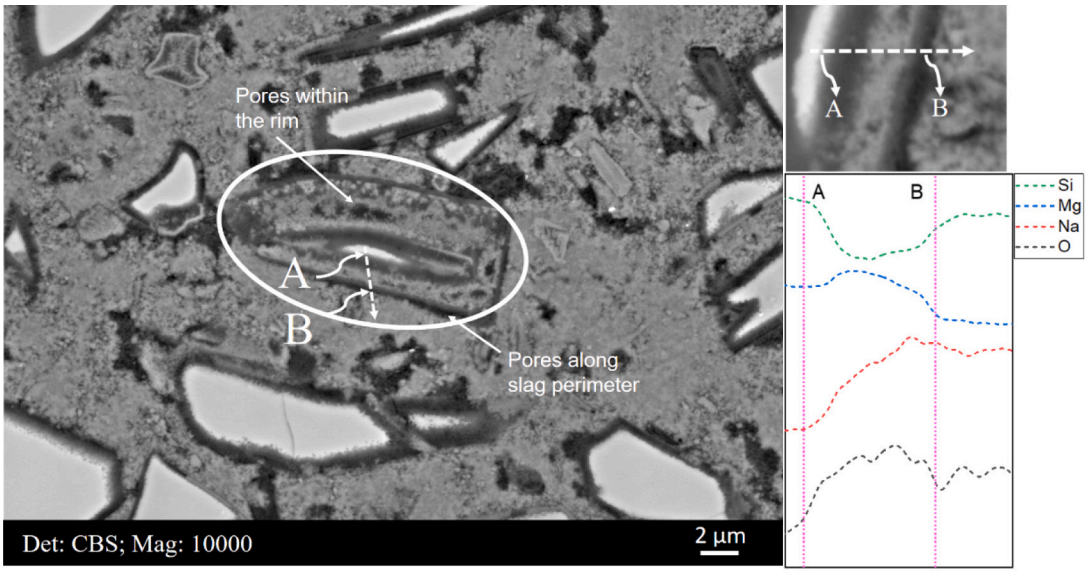

(a) (b)

Fig. 14. (a) A typical slag rim after CO_2 ingress; (b) Linescan-profiles of Si, Mg, Na, and O along the dissection lines A-B in (a).

illustrated in Fig. 15(c). Notably, the thin slice employed for TEM analysis had been distorted after milling, and continuous cracks were developed just below the sample surface. Compared to sealed curing, carbonation reduced the micro-mechanical properties of gel matrix, and thus it was more vulnerable to the damage induced by FIB. Moreover, pores in the range of microns were created in the rim. When zoomed in image of the area P1, both globular and foil/fiber-like morphology of the C-(N-)A-S-H gel phases can be found (Fig. 15(d)). As for area P2, numbers of lath-like precipitations, indicating the formation of hydration-like phase, were detected in it (Fig. 15(e)). They were more clearly exhibited in Fig. 15(e-1). The high-resolution fringes observed in Fig. 15(e-2) were indicative of the layered structure of this phase.

Fig. 16 presents a close-up HAADF micrograph of a representative region in Fig. 15(c), as well as the main element mappings containing pores, C-(N-)A-S-H gel phases, and hydrotalcite-like phase. As can be seen, some signals of Si and Al were detected in the pores. It was probably related to the formation of silica gel in it, originated from the (partial) carbonation of C-(N-)A-S-H gel phases. Al and Mg were accumulated in the middle to form hydrotalcite-like phase, agreed well with the morphology observation in Fig. 15(e). Calcium was detected on both sides close to Mg-rich region (circled in the Ca mapping). As for Si and Al, they were distributed across the whole region.

Compared to the rim analyzed in Fig. 5, the regular distribution pattern of inner products was modified because of carbonation, and pores were created in it. No enrichment of hydrotalcite-like phase near the boundary was detected anymore; however, its crystalline form did form within the rim.

3.5. *Transformation mechanism between these two types of zonation*

Based on the observations and discussion above, it was assumed in the present paper that the multi-ring zonation (Type II) cannot be formed from slag activation under sealed curing along. Instead, it was the massive formation of capillary pore in the range of 10 to 100 nm along slag perimeter, resulted from external intervenes, e.g., carbonation and leaching (a similar degradation mechanism with carbonation [21]), that triggered the reorganization of original distribution pattern of inner hydration products (Type I). As a result, this concentric ring structure was formed in the slag rim ultimately, irrespective of l/b ratio, pH of pore solution, etc.

The schematic illustration of the transformation routine between these two types of zonation is given in Fig. 17. We considered the situation shown in Fig. 14 as a precursor/intermediate/transition state for the multi-ring phenomenon.

In our previous work [26], Lifshitz-Slyozov instability [38] was employed to explain the distribution pattern of slag hydration products in a cement-based system. It was considered that larger, more stable hydrotalcite-like phase crystals grew at the expense of the smaller ones. Thus, a band/ring was formed where these large and stable crystals were concentrated, i.e., near the boundary. This process was also known as Ostwald ripening [45]. It was not inconceivable that this mechanism also applicable for AAS system that underwent sealed curing as observed in Section 3.1. Meanwhile, the larger the size of a slag grain, the harder it was for the newly released magnesium ion from the reaction front to reach the boundary due to its low mobility and increased migration distance. Therefore, it accumulated locally and formed an additional Mg-rich region that was in the core or connected to the unreacted slag particle. Note that the quantitative correlation between slag grain size and distribution pattern of inner hydrates (type I) was not given here, as it was not the main goal of this paper.

Revisiting the concentric ring structure observed in Section 3.2, the formation mechanism changed accordingly. As discussed in [42], the authors believed that the formation of multi-ring in the AAS systems can be a consequence of chemical differences between unreacted slag core and pore solution. Also, the generation of supersaturation–depletion cycle promoted the thickening of rings. Meanwhile, the results in the current study revealed that this concentric ring structure cannot be observed in AAS pastes with sealed curing no matter with a low (0.5) or a high (1.0) l/b ratio. The curing condition provided ('…, specimens were stored in an open laboratory facility in the Universidad del Valle, Cali, Colombia, for 7 years.') also confirmed that naturally exposed curing was implemented for the investigated samples, and they had been carbonated considering the high carbonation rate of AAS paste [44,57]. Therefore, the crucial role of capillary pore formed due to carbonation should be reconsidered, for the multi-ring phenomenon occurred in the rim of slag.

With the mass formation of capillary pores in the range of 10 to 100 nm in the carbonated specimens, the capillary condensation of pore solution was enhanced according to the Kelvin equation following [58]:

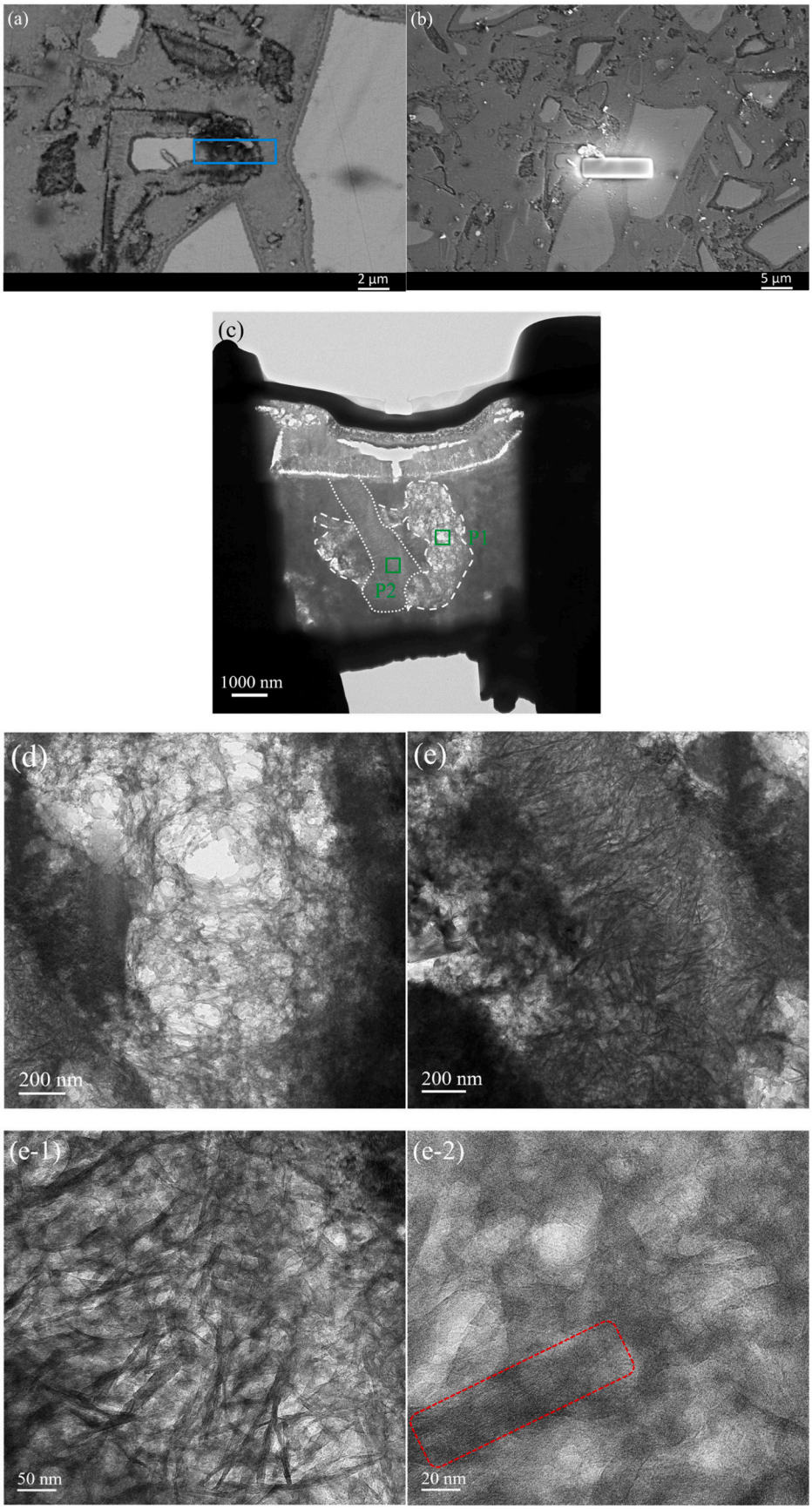

Fig. 15. TEM analysis of hydrates in the slag rim after CO_2 attack; (a) the BSE image of interested area; (b) coating the area with platinum cover; (c) the overall morphology of this typical slag rim beneath the platinum cover; (d) magnified image of the area P1 in (c); (e) zoomed in image of the area P2 in (c); (e-1) enlarged image of (e); (e-2) high-resolution lattice fringe image of hydrotalcite-like phase.

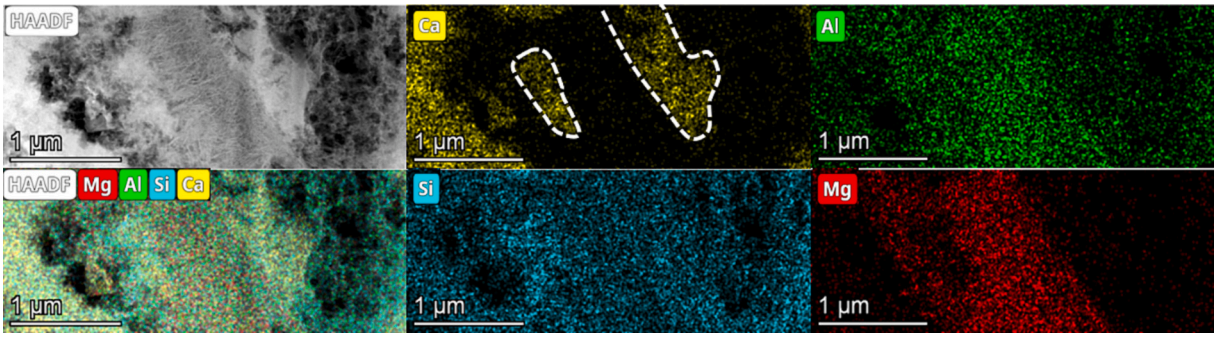

Fig. 16. The HAADF micrograph and main element mappings of Ca, Si, Al, and Mg of typical area containing pores, C-(N-)A-S-H gel phases, and hydrotalcite-like phase.

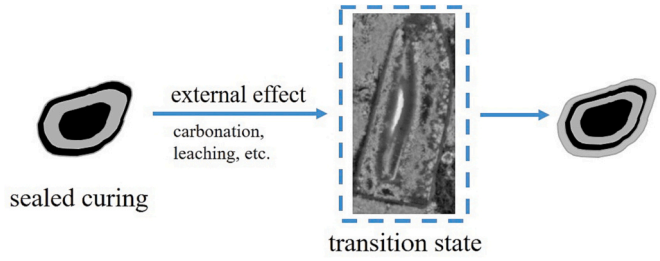

Fig. 17. A schematic illustration of the transformation routine between these two types of zonation.

$$RTln\,P/P_0 = -\frac{2\gamma V}{r}cos\theta$$

where P is the equilibrium partial pressure of water vapor in a capillary pore of radius r at the temperature T (K), P_0 is the saturated water vapor pressure, γ and V are the surface tension and molar volume of liquid water, respectively, R is the gas constant and θ is the contact angle between liquid water and pore surface. With increasing pore diameter from gel pore to capillary pore level, the molar volume of liquid water (or pore solution) condensed on the pore wall went up accordingly. Condensed pore solution with nearly neutral pH was adsorbed on capillary pores along slag perimeter, and it accelerated the dissolution of hydrotalcite-like phase (through Mg^{2+} leaching) precipitated near the boundary [59]. At the same time, carbonate ions were able to diffuse into slag rim and react with C-(N-)A-S-H gel phases formed inside the rim. Thus, the original distribution pattern of hydration products within the rim changed. At this stage, Ca^{2+} ions (the remnant from calcium carbonate precipitation), $SiO(OH)_3^-$ and $Al(OH)_4^-$ ions (decomposition of gel phases), as well as Mg^{2+} ions (leached from hydrotalcite-like phase) can migrate relatively freely in the rim owing to the enhanced porosity (see Fig. 14). This stage can be considered as the precursor/intermediate/transition state for the multi-ring phenomenon and was most frequently observed in the microstructure of carbonated AAS specimens.

Due to the free migration of cations in the slag rim, sufficient supersaturations of C-(N-)A-S-H gel phases and hydrotalcite-like phase resulted in localized high nucleation rates. In consequence, C-(N-)A-S-H gel phases and hydrotalcite-like phase would precipitate. High supersaturations and nucleation rates can induce the formation of numerous randomly distributed nanometer-sized colloidal C-(N-)A-S-H gel phases and hydrotalcite-like particles. With the movement of reaction-diffusion front, development of successive hydrotalcite-like phase-rich rings (rich in Mg, appears relatively dark) was separated by C-(N-)A-S-H gel phases bands (rich in Ca and deficient in Mg). Finally, they contributed to the multi-ring phenomenon observed in Section 3.2, as discussed in [42].

All in all, the development of multi-ring phenomenon in the carbonated (both natural and accelerated) AAS pastes starts with the dissolution of hydrotalcite-like phase by pore solution condensed in the capillary pores along the slag perimeter. The carbonation of C-(N-)A-S-H gel phase in the slag rim and thus the formation of pores in it enables the free diffusion of cations. Then, the moving reaction fronts of C-(N-)A-S-H gel phases and hydrotalcite-like phase contribute to this type of zonation within the slag rim. Additionally, it should be addressed that the slag rim should be thick enough for the formation of alternative rings. Therefore, this concentric ring structure is rarely detected in early-age specimens. Meanwhile, note that the correlation between slag grain size and concentric ring structure (type II) is out of the scope of this paper, which is different from the work in [26]. This is partially because the phenomenon is not universally applicable to every single slag grain, and most slag rims are in chaotic after carbonation, before reaching an equilibrium state. With this reason, these two types of zonation commonly coexist in the carbonated samples (see Figs. 7 and 9(a)). However, they are featured by different microstructures. As mentioned, multi-ring phenomenon is developed along with the massive formation of capillary pores in the 10 to 100 nm range. These pores are commonly produced owing to external effects, e.g., carbonation, leaching [60], etc., and offer passage for the transport of harmful ions, such as carbonate, chloride, sulfate, etc. Therefore, the occurrence of multi-ring phenomenon can be regarded as an indicator for the potential durability-related problems of AAS systems.

4. Conclusions

In the present research, the authors classified two types of zonation within the rims of slag under different curing conditions (sealed, naturally exposed, and accelerated carbonation) with the techniques of SEM and TEM. The main conclusions were drawn as follows:

- For the first type of zonation occurring in the rim of slag under sealed curing, it was found that magnesium was accumulated near the boundary, leading to the precipitation of lath-like hydrotalcite-like phase. Next, a generally fine, homogeneous, and foil-like morphology was noted, i.e., C-(N-)A-S-H gel phases. When slag rim was thick enough, a new region also rich in Mg occurred in the core or surrounding the unreacted slag grain.
- In the carbonated AAS pastes (naturally exposed and accelerated carbonation), a multi-ring phenomenon occurred within the slag rim (the second type of zonation). For this kind of distribution pattern, foil-like C-(N-)A-S-H gel phases, rather than hydrotalcite-like phase, was noted near the initial boundary of slag grain. The accumulation of Mg and Ca occurred alternatively in the following sub-zones. Globular C-(N-)A-S-H gel phases were also identified inside slag rim, probably originated from the (partial) carbonation of gel phases.
- It was proposed in the present study that external intervenes, e.g., carbonation, leaching, etc., played a crucial role for the occurrence of multi-ring phenomenon in the slag rim. The development of this concentric ring structure started with the dissolution of hydrotalcite-

like phase originally precipitated near the boundary by pore solution condensed in capillary pores along slag perimeter. Subsequently, the carbonation of C-(N-)A-S-H gel phases in the rim and thus the formation of pores in it enabled the relatively free migration of various cations. This stage can be regarded as a transition state, precursor, or intermediate. Finally, a pre-nucleation model involving cyclic supersaturation-crystallization-depletion of C-(N-)A-S-H gel phases and hydrotalcite-like phase was introduced to explain the final formation of this multi-ring phenomenon.

- Multi-ring phenomenon was developed along with the massive formation of capillary pores in the 10 to 100 nm range both along slag perimeter and inside the rim. These pores offer passage for the transport of harmful ions, such as carbonate, chloride, sulfate, etc. Therefore, the occurrence of multi-ring phenomenon can be regarded as an indicator for the potential durability-related problems of AAS systems.

CRediT authorship contribution statement

Yu Zhang: Investigation, Methodology, Experiment, Analysis, Writing - Original Draft preparation, Writing - Review & Editing.
Shizhe Zhang: Methodology, Analysis, Review & Editing.
Chen Liu: Experiment, Analysis, Review & Editing.
Oğuzhan Çopuroğlu: Supervision, Review & Editing.

Declaration of competing interest

The authors declare that they have no known competing financial interests or personal relationships that could have appeared to influence the work reported in this paper.

Data availability

Data will be made available on request.

Acknowledgements

Fundamental Research Funds for the Central University (Grant Number RF1028623287) is gratefully acknowledged for the financial support. Marija Nedeljković (Microlab, TU Delft) shared the old alkali-activated slag pastes for investigations, the authors would also like to thank her. Xuefeng Zhang from shiyanjia lab (www.shiyanjia.com) is greatly appreciated for his help on FIB-SEM system.

References

[1] Y. Yang, K. Raipala, L. Holappa, Ironmaking, in: Treatise on Process Metallurgy, Elsevier, 2014.
[2] J. Bijen, Benefits of slag and fly ash, Construct. Build Mater. 10 (5) (1996) 309–314.
[3] M. Juenger, et al., Advances in alternative cementitious binders, Cem. Concr. Res. 41 (12) (2011) 1232–1243.
[4] Y. Li, et al., Environmental impact analysis of blast furnace slag applied to ordinary Portland cement production, J. Clean. Prod. 120 (2016) 221–230.
[5] S.D. Wang, et al., Alkali-activated slag cement and concrete: a review of properties and problems, Adv. Cem. Res. 7 (27) (1995) 93–102.
[6] P. Duxson, et al., Geopolymer technology: the current state of the art, J. Mater. Sci. 42 (9) (2007) 2917–2933.
[7] B. Singh, et al., Geopolymer concrete: a review of some recent developments, Construct. Build Mater. 85 (2015) 78–90.
[8] C. Shi, D. Roy, P. Krivenko, Alkali-activated Cements and Concretes, CRC press, 2003.
[9] J. Skibsted, R. Snellings, Reactivity of supplementary cementitious materials (SCMs) in cement blends, Cem. Concr. Res. 124 (2019), 105799.
[10] K.C. Newlands, et al., Early stage dissolution characteristics of aluminosilicate glasses with blast furnace slag- and fly-ash-like compositions, J. Am. Ceram. Soc. 100 (5) (2017) 1941–1955.
[11] R. Snellings, C. Jantzen, Solution-controlled dissolution of supplementary cementitious material glasses at pH 13: the effect of solution composition on glass dissolution rates, J. Am. Ceram. Soc. 96 (8) (2013) 2467–2475.
[12] M. Zajac, et al., Late hydration kinetics: indications from thermodynamic analysis of pore solution data, Cem. Concr. Res. 129 (2020), 105975.
[13] W. Chen, H. Brouwers, The hydration of slag, part 2: reaction models for blended cement, J. Mater. Sci. 42 (2) (2007) 444–464.
[14] I. Richardson, et al., The characterization of hardened alkali-activated blast-furnace slag pastes and the nature of the calcium silicate hydrate (CSH) phase, Cem. Concr. Res. 24 (5) (1994) 813–829.
[15] A. Brough, A. Atkinson, Sodium silicate-based, alkali-activated slag mortars: part I. Strength, hydration and microstructure, Cem. Concr. Res. 32 (6) (2002) 865–879.
[16] M.B. Haha, et al., Influence of slag chemistry on the hydration of alkali-activated blast-furnace slag—part I: effect of MgO, Cem. Concr. Res. 41 (9) (2011) 955–963.
[17] M.B. Haha, et al., Influence of slag chemistry on the hydration of alkali-activated blast-furnace slag—part II: effect of Al2O3, Cem. Concr. Res. 42 (1) (2012) 74–83.
[18] S. Zhang, et al., Waste glass as partial mineral precursor in alkali-activated slag/fly ash system, Cem. Concr. Res. 102 (2017) 29–40.
[19] I. Richardson, G. Groves, Microstructure and microanalysis of hardened cement pastes involving ground granulated blast-furnace slag, J. Mater. Sci. 27 (22) (1992) 6204–6212.
[20] I. Richardson, G. Groves, The structure of the calcium silicate hydrate phases present in hardened pastes of white Portland cement/blast-furnace slag blends, J. Mater. Sci. 32 (18) (1997) 4793–4802.
[21] I. Richardson, Tobermorite/jennite-and tobermorite/calcium hydroxide-based models for the structure of CSH: applicability to hardened pastes of tricalcium silicate, β-dicalcium silicate, Portland cement, and blends of Portland cement with blast-furnace slag, metakaolin, or silica fume, Cem. Concr. Res. 34 (9) (2004) 1733–1777.
[22] R. Taylor, I. Richardson, R. Brydson, Composition and microstructure of 20-year-old ordinary Portland cement–ground granulated blast-furnace slag blends containing 0 to 100% slag, Cem. Concr. Res. 40 (7) (2010) 971–983.
[23] I. Richardson, S. Li, Composition and structure of an 18-year-old 5M KOH-activated ground granulated blast-furnace slag paste, Construct. Build Mater. 168 (2018) 404–411.
[24] H. Ye, Nanoscale attraction between calcium-aluminosilicate-hydrate and Mg-Al layered double hydroxides in alkali-activated slag, Mater Charact 140 (2018) 95–102.
[25] Z. Jia, et al., The characteristics and formation mechanism of the dark rim in alkali-activated slag, Cement and Concrete Composites 112 (2020), 103682.
[26] B. Li, Q. Li, W. Chen, Spatial zonation of a hydrotalcite-like phase in the inner product of slag: new insights into the hydration mechanism, Cem. Concr. Res. 145 (2021), 106460.
[27] Y. Zhang, O. Çopuroğlu, Role of the grain size on the hydration characteristics of slag in an aged field concrete, Cem. Concr. Res. 162 (2022), 106985.
[28] S.A. Bernal, et al., Natural carbonation of aged alkali-activated slag concretes, Mater. Struct. 47 (2014) 693–707.
[29] P. Ortoleva, The self organization of Liesegang bands and other precipitate patterns, in: Chemical Instabilities, Springer, 1984, pp. 289–297.
[30] H.K. Henisch, Crystals in Gels and Liesegang Rings, Harvard, 1988.
[31] K.H. Stern, The Liesegang phenomenon, Chem. Rev. 54 (1) (1954) 79–99.
[32] G. Dee, Patterns produced by precipitation at a moving reaction front, Phys. Rev. Lett. 57 (3) (1986) 275.
[33] D. Feinn, et al., Spontaneous pattern formation in precipitating systems, J. Chem. Phys. 69 (1) (1978) 27–39.
[34] R. Lovett, P. Ortoleva, J. Ross, Kinetic instabilities in first order phase transitions, J. Chem. Phys. 69 (3) (1978) 947–955.
[35] G. Venzl, J. Ross, Nucleation and colloidal growth in concentration gradients (Liesegang rings), J. Chem. Phys. 77 (3) (1982) 1302–1307.
[36] R. Feeney, et al., Periodic precipitation and coarsening waves: applications of the competitive particle growth modela, J. Chem. Phys. 78 (3) (1983) 1293–1311.
[37] J. Kirkaldy, Spontaneous evolution of spatiotemporal patterns in materials, Rep. Prog. Phys. 55 (6) (1992) 723.
[38] I.M. Lifshitz, V.V. Slyozov, The kinetics of precipitation from supersaturated solid solutions, Journal of Physics Chemistry of Solids 19 (1–2) (1961) 35–50.
[39] S.A. Rodger, G.W. Groves, The microstructure of tricalcium silicate/pulverized-fuel ash blended cement pastes, Adv. Cem. Res. 1 (2) (1988) 84–91.
[40] S. Bae, et al., Characterization of morphology and hydration products of high-volume fly ash paste by monochromatic scanning X-ray micro-diffraction (μ-SXRD), Cem. Concr. Res. 59 (2014) 155–164.
[41] F. Glasser, Chemical, mineralogical and micro-structural changes occurring in hydrated slag-cement blends, Material Science of Concrete (1991) 41–82.
[42] R. San Nicolas, et al., Distinctive microstructural features of aged sodium silicate-activated slag concretes, Cem. Concr. Res. 65 (2014) 41–51.
[43] Z. Shi, et al., Effect of alkali dosage and silicate modulus on carbonation of alkali-activated slag mortars, Cem. Concr. Res. 113 (2018) 55–64.
[44] M. Nedeljković, et al., Carbonation resistance of alkali-activated slag under natural and accelerated conditions, Journal of Sustainable Metallurgy 4 (1) (2018) 33–49.
[45] W. Dunning, Ripening and Ageing Processes in Precipitates, 1973.
[46] S. Song, H.M. Jennings, Pore solution chemistry of alkali-activated ground granulated blast-furnace slag, Cem. Concr. Res. 29 (2) (1999) 159–170.
[47] S. Song, et al., Hydration of alkali-activated ground granulated blast furnace slag, J. Mater. Sci. 35 (1) (2000) 249–257.
[48] V. Živica, Effects of type and dosage of alkaline activator and temperature on the properties of alkali-activated slag mixtures, Construct. Build Mater. 21 (7) (2007) 1463–1469.
[49] S. Aydın, B. Baradan, Effect of activator type and content on properties of alkali-activated slag mortars, Compos. Part B Eng. 57 (2014) 166–172.
[50] V. Ngala, C. Page, Effects of carbonation on pore structure and diffusional properties of hydrated cement pastes, Cem. Concr. Res. 27 (7) (1997) 995–1007.

[51] J.J. Chen, et al., Solubility and structure of calcium silicate hydrate, Cem. Concr. Res. 34 (9) (2004) 1499–1519.
[52] M. Nedeljković, et al., Effect of natural carbonation on the pore structure and elastic modulus of the alkali-activated fly ash and slag pastes, Construct. Build Mater. 161 (2018) 687–704.
[53] Markus Schönlein, Johann Plank, A TEM study on the very early crystallization of C-S-H in the presence of polycarboxylate superplasticizers: transformation from initial C-S-H globules to nanofoils, Cem. Concr. Res. 106 (2018) 33–39.
[54] X. Liu, et al., Carbonation behavior of calcium silicate hydrate (C-S-H): its potential for CO_2 capture, Chem. Eng. J. 431 (2022), 134243.
[55] Q. Feng, E. Lachowski, F. Glasser, Densification and migration of ions in blast furnace slag-portland cement pastes, MRS Online Proceedings Library Archive 136 (1988).
[56] J.L. Provis, et al., X-ray microtomography shows pore structure and tortuosity in alkali-activated binders, Cem. Concr. Res. 42 (6) (2012) 855–864.
[57] T. Bakharev, J. Sanjayan, Y.-B. Cheng, Resistance of alkali-activated slag concrete to carbonation, Cem. Concr. Res. 31 (9) (2001) 1277–1283.
[58] A.W. Adamson, A.P. Gast, Physical Chemistry of Surfaces 15, Interscience publishers New York, 1967.
[59] C. Foster, et al., Hydrotalcite colloidal stability and interactions with uranium(VI) at neutral to alkaline pH, Langmuir 38 (8) (2022) 2576–2589.
[60] C. Liu, et al., Degradation of alkali-activated slag subjected to water immersion, Cem. Concr. Compos. 142 (2023), 105157.